APL Photonics

# 500 GHz plasmonic Mach-Zehnder modulator enabling sub-THz microwave photonics

Cite as: APL Photonics 4, 056106 (2019); https://doi.org/10.1063/1.5086868
Submitted: 24 December 2018 • Accepted: 26 April 2019 • Published Online: 30 May 2019

Maurizio Burla, Claudia Hoessbacher, Wolfgang Heni, et al.

# 500 GHz plasmonic Mach-Zehnder modulator enabling sub-THz microwave photonics

Cite as: APL Photon. 4, 056106 (2019); doi: 10.1063/1.5086868
Submitted: 24 December 2018 • Accepted: 26 April 2019 •
Published Online: 30 May 2019



Maurizio Burla,[1,a] Claudia Hoessbacher,[1] Wolfgang Heni,[1] Christian Haffner,[1] Yuriy Fedoryshyn,[1] Dominik Werner,[1] Tatsuhiko Watanabe,[1] Hermann Massler,[2] Delwin L. Elder,[3] Larry R. Dalton,[3] and Juerg Leuthold[1]

## AFFILIATIONS

[1]Institute of Electromagnetic Fields, ETH Zurich, Gloriastrasse 35, Zurich 8092, Switzerland
[2]Fraunhofer IAF, Tullastraße 72, 79108 Freiburg im Breisgau, Germany
[3]Department of Chemistry, University of Washington, Seattle, Washington 98195-1700, USA

[a]**Author to whom correspondence should be addressed:** maurizio.burla@ief.ee.ethz.ch

## ABSTRACT

Broadband electro-optic intensity modulators are essential to convert electrical signals to the optical domain. The growing interest in terahertz wireless applications demands modulators with frequency responses to the sub-terahertz range, high power handling, and very low nonlinear distortions, simultaneously. However, a modulator with all those characteristics has not been demonstrated to date. Here, we experimentally demonstrate that plasmonic modulators do not trade-off any performance parameter, featuring—at the same time—a short length of tens of micrometers, record-high flat frequency response beyond 500 GHz, high power handling, and high linearity, and we use them to create a sub-terahertz radio-over-fiber analog optical link. These devices have the potential to become a new tool in the general field of microwave photonics, making the sub-terahertz range accessible to, e.g., 5G wireless communications, antenna remoting, Internet of Things, sensing, and more.



## I. INTRODUCTION

Microwave photonic applications in the terahertz range are recently attracting a growing interest due to the need to find solutions for next-generation (5G) wireless communication systems capable of unprecedented data rates. Over the last few years, in fact, we have seen an explosive growth of wireless data traffic, driven by widespread adoption of high-bandwidth services on mobile devices.[1] To enable the expected transmission rates of tens or even hundreds of Gb/s, carrier frequencies in the unallocated regions of the electromagnetic spectrum above 300 GHz are being considered[1–5] [Fig. 1(a)]. In fact, transmission rates in the widely used microwave bands are restricted by the limited allocated spectra—which typically amount to a few 100 MHz. Wider spectral bands have been opened up at millimeter-wave frequencies in the 60 GHz and the 70–95 GHz range; however, the contiguous bandwidth available in these bands is less than 9 GHz, which is still insufficient to support wireless data transmission at the desired speeds of hundreds of Gb/s without employing very high spectral efficiency modulation formats in the order of 512-QAM, which may be difficult to realize at several Gbaud symbol rates without drastically reducing link length.[1] As a consequence, higher carrier frequencies must be looked into, in particular, at currently unallocated regions of the spectrum above 300 GHz. To some, the terahertz band (300 GHz–10 THz) is considered as the "next frontier" to meet the future data target thanks to an extremely large bandwidth available.[5] However, important challenges appear when entering this spectral region, which require different system architecture compared to omnidirectional wireless transmission. First, free space path loss increases as the square of the frequency and must be compensated using directional transmitters such as high-gain steerable phased arrays; on the other hand, atmospheric absorption due to water vapor becomes a problem. Nonetheless, several spectral windows between 200 and 450 GHz with reduced absorption exist.

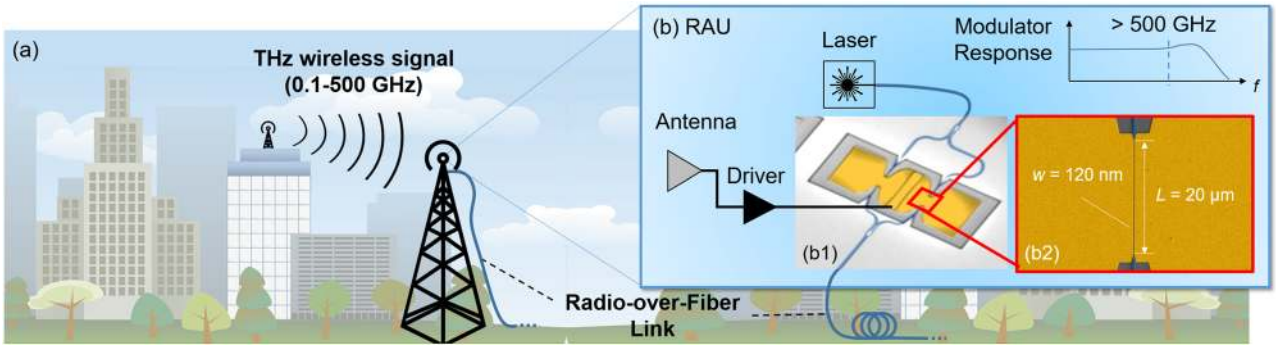


**FIG. 1**. (a) A THz wireless communication scenario. (b) At the remote antenna unit (RAU), THz wireless signals are received by an antenna and converted to the optical domain to be transported over a radio-over-fiber analog link. A modulator with sub-THz bandwidth, high linearity, and high-power handling is needed to encode the THz signal onto an optical carrier with high fidelity. Inset: (b1) micrograph of a plasmonic Mach-Zehnder modulator with a plasmonic phase modulator in each arm; (b2) image of the 120 nm-wide, 20 $\mu$m-long phase modulator slot waveguide (background image: edited from https://pixabay.com/).

Since each of these windows offers several tens of gigahertz bandwidth, they are suitable for wireless links with ultra-high capacity for distances in the order of 100 m.[1]

Terahertz signals above 300 GHz can be generated and detected either using all-electronic devices[6,7] or via photonic techniques.[4,5,8,9] Since the backbone of the internet is composed by very high-capacity fiber optic cables, the photonic approach has the ultimate advantage to allow seamless integration with the existing fiber networks.[4] This, however, requires optical-to-terahertz and terahertz-to-optical converters with bandwidth well above 300 GHz, high power handling and high linearity. While uni-traveling-carrier photodiodes (UTC-PD) are an established solution for optical-to-terahertz conversion,[5] including integration with sub-terahertz waveguides,[10] efficient terahertz-to-optical conversion is still a challenge for the radio-over-fiber community[11–13] as it requires modulators with electro-optic bandwidth well above 300 GHz, high power handling and very high linearity,[14] which have not been demonstrated to date in any single device. In addition, besides terahertz communications, such modulators would potentially enable many more applications to reach the terahertz frequency range, such as high-speed airborne millimeter-wave photonic relays,[15] agile millimeter-wave communication using photonic frequency conversion,[16] signal distribution for millimeter-wave satellite instrumentation,[17] photonic signal processing of radio signals[18] or millimeter-wave radar.[19,20]

Current modulators optimized for analog applications are mostly based on lithium niobate,[21] gallium arsenide,[22] indium phosphide[23] and, more recently, silicon.[24] Those devices have shown good performance in terms of linearity and power handling; however, commercial solutions require large millimeter- or even centimeter-scale traveling wave structures for broadband performance and are limited to speeds below 110 GHz. Very recently, impressive progress has been made in lithium niobate modulators. Weigel *et al.* have shown modulators[25] with a 3-dB bandwidth beyond 106 GHz, realized by oxide-bonding a thin-film of $LiNbO_3$ to a foundry-fabricated silicon photonic circuit. Mercante *et al.* successfully demonstrated a thin film crystal ion sliced (CIS) $LiNbO_3$ phase modulator.[26] By precise index matching between the co-propagating optical and RF modes, they were able to extract a measurable electro-optical response up to 500 GHz, with a measured DC half-wave voltage of 3.8 V $cm^{-1}$. Wang *et al.* have shown an integrated lithium niobate-on-insulator (LNOI) Mach–Zehnder optical modulator[27] with a 3-dB bandwidth of 40 GHz, a length of the order of 20 mm, a device loss of only 0.5 dB, and an ultra-low RF half-wave voltage of 1.4 V. The same authors also reported a version with 100 GHz bandwidth and a $V_\pi L$ of 2.2 V cm. All these devices show very strong potential for microwave photonic systems and next-generation optical communication networks.[28] Over the last four years, a novel class of modulators, known as plasmonic modulators, has been introduced and demonstrated ultracompact footprints[29] (10 s $\mu m^2$), ultralow power consumption (2.8 fJ/bit at 100 GBd),[30] and flat frequency responses up to 170 GHz[31] and 325 GHz.[32] Interestingly, in most recent structures, reasonably low loss were reported [2.5 dB in-chip losses for a ring modulator[29] and 8 dB for a Mach-Zehnder modulator (MZM)[33]]. Very recently, plasmonics has shown the ability to detect terahertz pulses using bow-tie shaped structures.[34] However, while all of these results are of highest interest, a modulator simultaneously displaying sub-terahertz frequency responses, high power handling, and high linearity has not yet been shown.

Here, we experimentally demonstrate plasmonic Mach-Zehnder modulators (MZMs) with a flat frequency response up to 500 GHz. The modulators are below 25 $\mu$m in length and display high linearity, with a third-order input intercept point (IIP3) of 18.9 dBm, in line with those of high-performance commercial modulators optimized for analog applications. In two-tone tests, they also display operation at high RF power level, up to 21.4 dBm (~138 mW) per tone (24.4 dBm in total, 276 mW), only limited by the power of the available RF amplifiers. We use them to demonstrate an analog radio-over-fiber (RoF) link up to 325 GHz, with >100 GHz bandwidth, only limited by our electrical measurement equipment. This indicates that plasmonic modulators have a strong potential not only for digital communications but they can also handle the stringent requirements needed for high-performance microwave photonics applications, communications, sensing, and more.

## II. 500 GHz MACH-ZEHNDER MODULATOR

Plasmonic modulators are based on the concept of surface plasmon polaritons (SPPs). SPPs are electromagnetic surface waves propagating at dielectric-metal interfaces.[35–37] For our modulators, we resort to the plasmonic organic hybrid (POH) platform.[38] A plasmonic phase modulator is depicted Fig. 1(b2). It consists of two metallic electrodes forming a metal-insulator-metal (MIM) slot waveguide. The slot is filled with a nonlinear organic material[39,40] whose refractive index changes linearly with the applied electric field, according to the Pockels effect.[41] A silicon strip waveguide (450 nm-wide, 220 nm-thick) feeds light to the plasmonic slot waveguide. A linear taper transforms the photonic mode in the silicon nanowire to a SPP that propagates along the slot, where its phase is modulated by the applied field and is then coupled back to the photonic waveguide by an identical output taper. High modulation indices are obtained thanks to the strong electrical and optical field confinement in the slot and an excellent overlap of the two fields. Thanks to the high modulation efficiency, the plasmonic slot can be kept short and, in turn, optical losses are reduced. A very important advantage of this kind of modulators for microwave photonics (MWP) applications is their ultrabroad electro-optical bandwidth due to the quasi-instantaneous nonlinear effect and the extremely small *RC* time constant of the structure. In fact, the small slot height and length reduce its capacitance to the femtofarad range, while the resistance is low (sub-1 Ω, neglecting the contact pads) thanks to the high conductivity of the metal electrodes. This yields a theoretical cutoff frequency in the terahertz range, according to theoretical predictions.[42] This, in turn, also enables operation in the millimeter-wave and subterahertz range as desired for MWP applications. In order to support high-frequency operation, the metallic electrical pads of the modulator are designed to be as small as possible while still allowing to electrically contact the device using the available probe, featuring a 50 $\mu$m pitch and a ground-signal-ground (GSG) configuration. Further details on the electrical modeling of the modulator are available in Ref. 43.

The device employed in the test is a POH-MZM,[44] Fig. 1(b1), composed by a silicon strip-waveguide interferometer with one 20 $\mu$m–long POH phase modulator in each arm [Fig. 1(b2)]. In this implementation, each phase modulator is realized with a ~120 nm-wide slot waveguide filled with the organic electro-optic material composite HD-BB-OH/YLD124.[40] This type of composites has shown electro-optic coefficients in POH devices reaching 325 pm/V when operating close to the resonance wavelength.[45] The phase modulators are driven in push-pull using a ground-signal-ground (GSG) electrical probe configuration. An extinction ratio of approximately 25 dB has achieved, indicating an accurate amplitude balance in the two arms of the Mach-Zehnder interferometer. Cut-back measurements show a loss for the unoptimized optical grating couplers of approximately 5 dB/coupler. Each photonic-plasmonic converter[42] displays a loss of approximately 1.1 dB. This allows us to estimate a loss in the plasmonic slot in the order of 0.5 dB/$\mu$m. The photonic-plasmonic converter is designed[46] as a linear taper having a length of 1 $\mu$m and narrowing down the 450 nm-wide silicon waveguide.

In the next step, we describe the experiments that have been performed to assess the frequency response of the POH-MZM to electrical signals from 75 MHz up to 500 GHz onto an optical continuous-wave (CW) carrier. In the experiments, a CW laser at 1547.5 nm with 0 dBm optical power was fed into the POH-MZM. The frequency response to the electrical signals were then

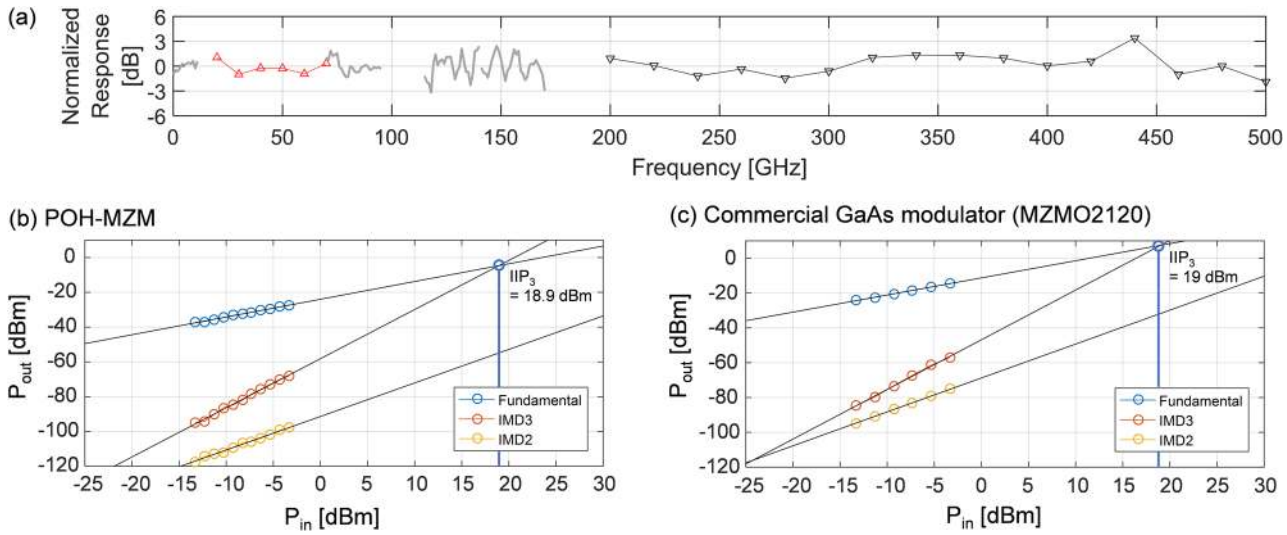


**FIG. 2.** (a) Measured response of the POH-MZM output for input frequency from 75 MHz to 500 GHz. The figure displays the measured power of the optical modulation sidebands, normalized to the electrical input power to the POH-MZM. The device features a flat response up to 500 GHz. [(b) and (c)] Second-order (IMD2) and third-order (IMD3) intermodulation distortions for the POH-MZM (a) and a commercial GaAs modulator (b). The horizontal axis indicates the available RF power at the modulator input generated by the source. The third-order input intercept point for the POH-MZM is at 18.9 dBm, very close to the 19.0 dBm obtained with a commercial high-performance GaAs modulator with the same half-wave voltage.

determined in two different setups that covered the frequency ranges from 15 GHz to 70 GHz and 200 GHz to 500 GHz. Subsequently, the optical spectrum of the intensity-modulated carrier at the modulator output was measured using an optical spectrum analyzer (OSA). The amplitude ratio between the fundamental and first side lobe in the spectrum was then used to determine the relative response of the electrical signal onto the optical signal.[47] The frequency response was then normalized with respect to the power of the electrical signal driving the modulator.

The results of the frequency response measurements are depicted in Fig. 2(a). The figure shows a flat frequency response from 75 MHz to 500 GHz, compiled from the two different setups as above. The response is flat with a ripple always below ±3 dB (the origin of the ripple is discussed in the supplementary material). As a consequence, we are not yet able to measure a bandwidth limitation since the response never crosses the −3 dB line compared to the low-frequency response. Additionally, we include (gray solid lines) the measurements from 75 MHz to 15 GHz, from 70 GHz to 95 GHz and from 115 GHz to 170 GHz, as reported by Hoessbacher *et al.*,[31] who obtained them with a similar POH-MZM device. Both measurements have been normalized to their low frequency value to show that this kind of modulators feature a flat frequency response over the complete measurable spectral region and show no signs of bandwidth limitation. Frequency ranges from 95 GHz to 115 GHz and from 170 GHz to 200 GHz cannot be covered in our laboratory.

Below 170 GHz, the test signal was generated by electrical means, using a signal generator and appropriate frequency multipliers. In the frequency range between 200 and 500 GHz, the test signal was generated by optical means via optical heterodyning, using two tunable laser sources and a UTC-PD to generate a terahertz signal at the frequency difference between the two lasers. The UTC-PD displays a 3 dB bandwidth in the 270 GHz–370 GHz range; however, it is still capable of generating signals down to 200 GHz and up to about 500 GHz. Full details on the experimental setups and the procedure used to measure the modulator response are reported in the supplementary material.

## III. LINEARITY AND POWER HANDLING

In analog photonic applications, linearity is a crucial parameter as it directly affects the system spurious-free dynamic range (SFDR).[14,48] The SFDR is a figure of merit that indicates the realistic power range over which a given network is capable of operating in a linear regime without being limited by noise.[14] For an intensity modulator, linear operation indicates that the modulating signal is transferred with high fidelity to the intensity of the light, i.e., without introducing any spurious frequency components. Deviations from the linear regime, e.g., generation of spurious tones, are known as nonlinear distortions. Those are important since, once generated, they normally can no longer be removed. In the following, we report the experimental characterization of the nonlinear distortions introduced by a POH-MZM. The results demonstrate that the nonlinear distortions from this modulator are in line with those of commercial Mach-Zehnder modulators optimized for analog photonic applications. The most common way to probe these nonlinear effects is the use of the method known as two-tone test.[48] This method allows us to characterize the second- and third-order intermodulation distortions (IMD2 and IMD3), which limit the SFDR in suboctave and multioctave conditions, respectively.[48] Importantly, however, the direct measurement of the SFDR value does not allow us to immediately draw conclusions on the linearity of the modulator alone because it includes the effects of noise and loss terms in the link. Therefore, in order to analyze nonlinear distortions originating from the modulator, we measure the IMD2 and IMD3 terms, as suggested in the literature.[48] Through this test, we could experimentally compare the linearity of the POH-MZM with the one of a commercial GaAs modulator optimized for high-performance analog applications ($U^2T$ model MZMO2120: $V_\pi$ = 3 V, an electro optical response of 33 GHz at 3 dB, a typical insertion loss of 5 dB, and a typical extinction ratio of 23 dB). The results in Figs. 2(b) and 2(c) show that the third-order intermodulation distortions from the POH-MZM are as low as those obtained from the commercial modulator.

Experimental two-tone tests are performed on the POH-MZM device with phase modulators having a slot length of 25 $\mu$m and a width of approximately 65 nm. Tests were performed at a frequency of 21 GHz ± 1 kHz (only limited by the available microwave components and test equipment), when the modulator is operated in its quadrature point, as discussed above, using a high power handling photodiode (PD). The quadrature operating point is established by measuring the DC half-wave voltage (conversion efficiency) of the modulator. Tests show a $V_\pi$ of 3 V; the DC-$V_\pi$ characteristic is reported in the supplementary material. The modulator is biased in quadrature using a voltage source, fed to the modulator using a bias-tee attached to the RF probe. The power at the PD input was kept at least 5 dB below its maximum to ensure that distortions originating from the PD are negligible. The power of the input tones is swept between −13.3 dBm and −3.3 dBm (corresponding to driving voltages ranging from 236 mV peak-to-peak to 744 mV peak-to-peak on this load). The corresponding powers of the fundamental ($f_1$, $f_2$), IMD2 ($f_1$+$f_2$), and IMD3 ($2f_1$-$f_2$ and $2f_2$-$f_1$) tones are measured with an electrical spectrum analyzer (ESA) and reported in Fig. 2, where the horizontal axis indicates the available RF power at the modulator input generated by the source. Details on the experimental setup are reported in the supplementary material.

The intercept point of the extrapolation of the fundamental and the IMD3 curve is known as third-order intercept point (IP3). The input power corresponding to this value (3rd order input intercept point, IIP3) amounts to 18.9 dBm. For comparison, we have measured a commercial GaAs modulator [$V_\pi$ = 3.0 V at 20 Gb/s pseudo-random bit sequence (PRBS)] using the same setup and the same average optical power impinging on the PD. The measured IIP3 in quadrature was 19.0 dBm. This result demonstrates that the linearity distortions originating from third-order intermodulations in POH-MZM are at least comparable to those obtained using commercial high-integrity modulators optimized for both telecom and radio-over-fiber applications.

Using current unoptimized grating couplers (~5 dB loss each) leads to a link gain in the order of −24 dB. This can be increased by reducing the optical propagation losses and the fiber-chip coupling losses, which could be improved, e.g., using more efficient grating couplers or edge coupling. We expect that an RF gain improvement of about 10 dB or more can be achieved by reducing coupling loss to state-of-the-art values of approximately 2.5 dB per grating.

Using the same setup, high RF power tests have also been performed. We employed two high power RF amplifiers to feed two signals simultaneously at 1 GHz. The modulator showed operation without damage up to 21.4 dBm (~138 mW, ~12.8 V peak-to-peak) of electrical input power for each tone—only limited by the power of the available RF amplifiers. We believe that the favorable higher power handling without any damage is due to the fact that—since the modulators are very short—we operate them by capacitive loading, where only little energy is dissipated in the capacitor itself. Also, an efficient heat dissipation is provided by the high thermal conductivity of the gold electrodes constituting the modulator slot. Further tests have also shown that the modulator can handle high optical input power. Nondestructive tests showed normal operation for on-chip optical input power up to at least 16 dBm. Taking into account the grating coupler losses provided above, the optical power impinging on the modulator input amounts to ~11 dBm. To put these values into context, we observe that analog photonic links benefit of high optical powers because the link gain of intensity-modulated links based on Mach-Zehnder modulators scales as the square of the optical carrier power.[14,48] Values in the range of 27 dBm have been used to achieve links with a record-high positive link gain of 44 dB.[49] At the same time, there is large consensus on the fact that, for a successful and effective adoption of microwave photonics solution in many real-life applications, a strong reduction in their size, weight, and power (SWaP) is required.[28,50–54] Toward this aim, state-of-the-art work has successfully managed to reduce the optical and RF power needed to implement microwave photonics functions (e.g., filtering and instantaneous frequency measurement) down to the 10–15 mW range.[52,55] All this, while at the same time providing much improved bandwidth, frequency flexibility (e.g., ultra broadband frequency tuning) and resolution[56] compared to all-electronic microwave systems. Other examples include low-power, fully programmable, on-chip RF-photonic processors as those shown, e.g., by Zhuang *et al.*[57] and Pérez *et al.*[58] Monolithically integrated demonstration of programmable microwave filters (Fandiño *et al.*[59]) has also been reported, operating with RF input power below 5 dBm and optical powers below −30 dBm. In most cases, those systems are designed for being employed in front-end of wireless receiving systems, where sensitivity is crucial and RF input power to the modulator is generally limited to a few dBm at best.[28,60] For these reasons, we believe that the RF and optical power handling of our modulator is well in line with the requirements for implementing next-generation integrated microwave photonic systems.

It is important to note that the POH-MZM generally presents a high reflection coefficient when connected to a 50 Ω transmission line and source, as done in our experiments. While it may seem counterintuitive, in practical applications, two important advantages stem from such impedance mismatch. First, since the modulator is based on Pockels effect, the desired refractive index variation in the waveguide is linear with the voltage drop on the modulator electrodes.[41] In case of impedance mismatch, a standing wave is

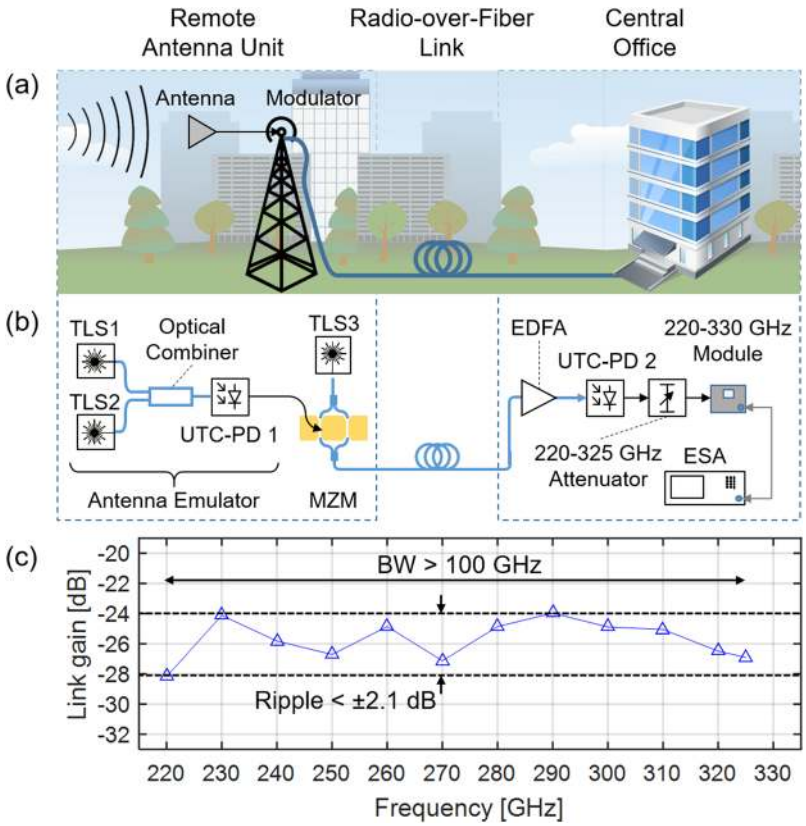


**FIG. 3**. (a) RoF link scenario connecting a remote antenna to a central office. (b) Experimental setup. (c) Measured link gain of the analog radio-over-fiber link. The link operates between 220 and 325 GHz, only limited by the available electrical test equipment (background image: edited from https://pixabay.com/).

created that induces a higher voltage magnitude (up to a factor 2, for a completely reflective load with an unitary reflection coefficient) on the modulator electrodes when compared to the case of perfect impedance matching.[61] Therefore, a higher electro-optic effect may be obtained with the same power available from the source (provided that the source is protected from potentially detrimental effects of those reflections). In addition, it is important to note that the high-impedance characteristics may be a very strong advantage when, for example, designing high-speed RF drivers for these modulators. In fact, the final stage of the amplifier/driver only needs to drive a nearly capacitive load, and this relaxes design constraints with respect to a circuit that must drive a 50 Ω load. Examples and further discussion on this regard are available in Refs. 62 and 63.

## IV. 325 GHz ANALOG RADIO-OVER-FIBER LINK

To further prove the capability of the modulator in Fig. 1, we use it to implement an analog RoF link, as depicted in Fig. 3(a), demonstrating direct terahertz-to-optical-to-terahertz conversion over >100 GHz bandwidth (220–325 GHz range), only limited by our electrical test equipment. The experiment shows that the link has a flat response over the complete 220–325 GHz frequency range. Figure 3(b) shows the setup, and Fig. 3(c) displays the broadband RoF link transmission response, normalized to the UTC-PD responsivity. As done for the modulator response test, sub-terahertz waves are generated using UTC-PD 1, emulating an antenna source, and are used to directly modulate an optical carrier using a POH-MZM [Fig. 3(b)]. The modulated signal propagates through a radio-over-fiber link. The received optical power is increased using a low-noise erbium-doped fiber amplifier (EDFA). The millimeter-waves are then detected with another UTC-PD and analyzed using an ESA with a millimeter-wave extension module. Further details on the setup and the calibration procedure are reported in the supplementary material. This experiment demonstrates the modulator capability to perform direct terahertz-to-optical conversion and confirms its flat response. Residual ±2.1 dB variations across the band are attributed to ripples in the attenuator loss, which could not be tested in our laboratory.

## V. CONCLUSIONS

We have experimentally demonstrated Mach-Zehnder modulators simultaneously meeting all requirements for analog applications, i.e., high linearity, high power handling, and speeds reaching 500 GHz. To our knowledge, we reported the fastest Mach-Zehnder modulator to date. We also demonstrate a radio-over-fiber link up to 325 GHz (>100 GHz bandwidth). These results suggest that plasmonics has the potential for becoming a new tool to the field of microwave photonics, enabling applications to reach the sub-terahertz range, while preserving the high-performance required in large-scale analog applications such as 5G wireless, antenna remoting, Internet of Things, sensing, and more.

## SUPPLEMENTARY MATERIAL

See supplementary material for details on the following aspects: experimental setups employed to measure the frequency response of the modulator (supplementary material, Sec. I); procedure used to extract the modulator response, discussion on conversion efficiency and techniques for reducing the half-wave voltage and loss in plasmonic modulators (supplementary material, Sec. II); details on the setup and procedure employed to measure the third-order intermodulation distortions via two-tone tests (supplementary material, Sec. III); detailed description of the setup employed the radio-over-fiber link experiment in the 220–325 GHz window (supplementary material, Sec. IV), calculation of the radio-over-fiber link response (supplementary material, Sec. V); details on device fabrication and nonlinear material stability (supplementary material, Sec. VI).

## ACKNOWLEDGMENTS

The authors wish to thank Professor C. Bolognesi, H. Benedikter, and M. Leich for support with the experiments and NTT for providing the UTC-PD. M. Burla acknowledges Dr. D. Marpaung for the fruitful discussions.

M. Burla acknowledges SNSF Ambizione Grant No. 173996. The authors acknowledge ERC PLASILOR Project No. 670478, H2020 PLASMOfab Project No. 688166, NSF (Grant No. DMR-1303080), and AFOSR (Grant No. FA9550-19-1-0069).

## APPENDIX: ESTIMATION OF NOISE FIGURE AND SPURIOUS-FREE DYNAMIC RANGE OF THE 325 GHz ANALOG LINK

In this Appendix, we describe how we can quantitatively estimate the noise figure (NF) and the spurious-free dynamic range of the realized 325 GHz analog link depicted in Fig. 3(b).

We wish to clarify that the scope of this work is neither noise reduction nor SFDR enhancement but linearity characterization of the modulator. However, while the SFDR optimization is beyond the scope of this specific work, for the sake of completeness, here we provide an estimation of the noise figure and of the SFDR values that we can expect by performing calculations based on measurement data. It is important to note that measuring the SFDR for the 325 GHz link is not trivial as it would require two high-power 325 GHz sources in order to measure nonlinear distortions (using the setup displayed in Fig. S3), which are not available to us.

### 1. Analog optical links based on Mach-Zehnder modulator

A microwave photonic link (MPL) or analog optical link (AOL) consists of a modulation device, used for electrical-to-optical conversion, which is connected via an optical fiber or optical waveguide to a photodetector, where the optical-to-electrical conversion occurs.[14] MPLs can be effectively used to transport very high-frequency electrical signals over large distances, leveraging the ultra-low loss of optical fibers. While different modulation schemes and techniques can be used in MPLs, the majority of links employed today are based on intensity modulation and direct detection (IMDD). Within this category, we can further divide links based on directly modulated lasers (DMLs) or external modulation via electro-optic modulators (EOMs). In our experiment, described in Sec. IV, we employed an IMDD based on external modulation using a Mach-Zehnder modulator. A schematic of a generic MPL based on external modulator is shown in Fig. 4(a). From an electrical perspective, an MPL is equivalent to a 2-port microwave network, as shown in Fig. 4(b).

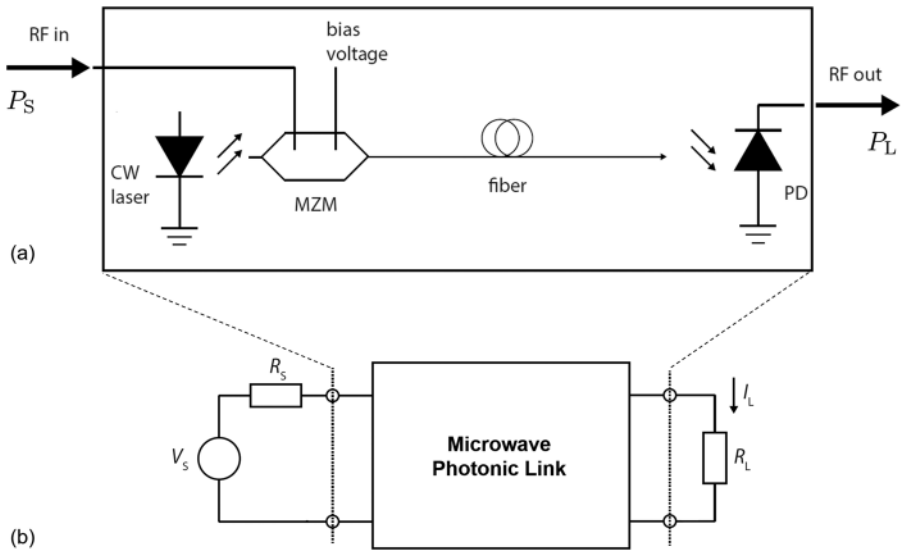


**FIG. 4**. Analog optical link represented as a 2-port microwave network.

The most important figures of merit of MPLs are the link gain ($g$), noise figure (NF), $n^{\text{th}}$-order input and output intercept points ($\text{IIP}_n$ and $\text{OIP}_n$), and spurious-free dynamic range (SFDR).

## 2. Link gain

The link gain of a MPL represents the RF-to-RF power signal transfer and is defined as the ratio between the power dissipated on the load and the power available from the source

$$g = \frac{P_L}{P_S}, \tag{A1}$$

which, in the hypothesis of maximum power transfer, can be expressed as[64]

$$g = \frac{P_L}{P_S} = \frac{\langle I_L^2(t)\rangle R_L}{\langle V_S^2(t)\rangle/4R_S}, \tag{A2}$$

where the acute brackets indicate a time average. The part of the load current contributing to the link gain is only the time-varying part, given by

$$I_L(t) = \frac{1}{2} r_{PD} P_{mod}(t), \tag{A3}$$

where $r_{PD}$ is the photodetector responsivity and $P_{mod}(t)$ is the time-varying component of the optical power on the photodetector. The latter depends, among others, on the modulation scheme used. In case of external modulation using a Mach-Zehnder modulator, the total optical power on the photodetector can be written as

$$P_{det,MZM}(t) = \frac{P_i}{2L}\left(1 - \cos\left[\pi\left(\frac{V_B}{V_{\pi,DC}} + \frac{V_{RF}(t)}{V_{\pi,RF}}\right)\right]\right), \tag{A4}$$

where $P_i$ is the input optical power to the modulator, $L$ is the optical loss of the link, $V_B$ is the modulator bias voltage, $V_{RF}(t)=V_S(t)/2$ is the modulating RF signal and $V_{\pi,DC}$ and $V_{\pi,RF}$ are the DC and the RF half-wave voltages of the modulator, respectively. Note that $L$ in the above equation comprises two terms, the modulator insertion loss, $L_{mod}$, and an excess loss, $L_{ex}$ (including fiber loss, connectors losses, etc.), such that $L = L_{mod}L_{ex}$.

In small signal regime, where $V_{RF} \ll V_{\pi,RF}$, the argument of the cosine can be expanded in a Taylor series as the sum of a DC term, $P_{av,MZM}$, plus terms which have a linear, quadratic and cubic dependence on the modulating signal $V_{RF}(t)$. For the link gain we only consider the contribution of the linear component:

$$P_{mod,MZM}(t) = \frac{P_i}{2L_{mod}} \frac{\pi V_{RF}(t)}{V_{\pi,RF}} \sin\varphi_B, \qquad \varphi_B \doteq \frac{\pi V_B}{V_{\pi,DC}}, \tag{A5}$$

where $L_{mod}$ is the insertion loss of the modulator and $\varphi_B$ is the bias angle. From the equations above, we obtain the expression of the link gain in a MZM externally-modulated MWP link:

$$g_{MZM} = \left(\frac{\pi r_{PD} R P_i \sin\varphi_B}{4LV_{\pi,RF}}\right)^2, \tag{A6}$$

where $r_{PD}$ is the photodetector responsivity, $R$ is the source and load resistance, $P_i$ is the optical power from the laser, $\varphi_B$ is the bias angle, $L$ is the total optical loss of the link, and $V_{\pi,RF}$ is the RF half-wave voltage of the modulator.

## 3. Noise figure

The noise figure (NF) of an MPL is defined as the noise factor ($F$) represented in decibel. The noise factor, in turn, is defined as the ratio between the signal-to-noise ratio at the input and the signal-to-noise ratio at the output of the link. The NF of a photonic link can then be written as[14]

$$\text{NF} = 10\log_{10}\left(\frac{S_{in}/N_{in}}{S_{out}/N_{out}}\right), \tag{A7}$$

where $S_{in}$ and $N_{in}$ are the input signal and noise power, respectively, and $S_{out}$ and $N_{out}$ are the output signal and noise power, respectively, expressed in watts. Considering the input noise power as the thermal noise $N_{in} = kTB$ ($k$ is the Bolzmann constant, $T$ is the ambient temperature, and $B$ is the noise equivalent bandwidth) and that

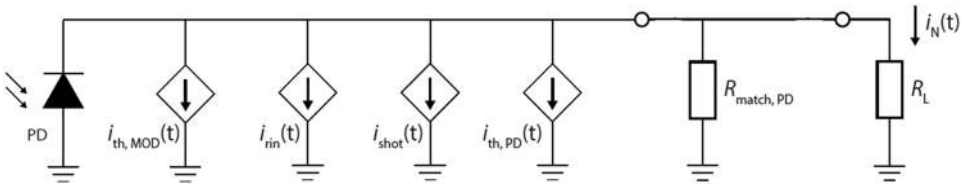


**FIG. 5**. Equivalent circuit model of a noisy microwave photonic link.

the output signal $S_{out}$ is simply the input signal power multiplied by the link gain, $S_{out} = g\,S_{in}$, the noise figure of the link can be rewritten as

$$\mathrm{NF} = 10\log_{10}\left(\frac{P_N}{gkTB}\right), \tag{A8}$$

where $P_N$ is the total noise power dissipated on the load. In a basic externally modulated photonic link, composed by a Mach-Zehnder modulator, a fiber link, and a photodetector, the total link noise power is given by the sum of different noise terms. In particular, the noise contributions are the thermal noise, the shot noise, the relative intensity noise (RIN) from the laser, and the thermal noise from the photodetector. These terms can be represented as random processes indicated by noise currents that add up to the photocurrent originating from the photodetector. This can be represented by the equivalent circuit in Fig. 5, where every noise source is represented by a "noisy" current source.

In detail, $i_{th,MOD}$ is the thermal noise current from the modulator, $i_{th,RIN}$ represents the relative intensity noise of the laser, $i_{shot}$ models the shot noise, and $i_{th,PD}$ is the thermal noise current from the photodetector. The total noise current flowing on the load is therefore

$$i_N(t) = \frac{1}{2}\left(i_{th,MOD}(t) + i_{shot}(t) + i_{rin}(t) + i_{th,PD}(t)\right). \tag{A9}$$

Based on this discussion, the total noise power dissipated on the load can be written according to the following equation:[14,64]

$$P_N = (1+g)P_{th} + \frac{1}{4}P_{shot} + \frac{1}{4}P_{rin}, \tag{A10}$$

where $P_{th}$ and $g\,P_{th}$ (lumped together) are the thermal noise powers originating from the modulator and from the photodetector, with $P_{th} = kTB$; the term $P_{rin}$ is the relative intensity noise (RIN) from the laser, given by

$$p_{rin} = 10^{\frac{RIN}{10}} I_{av}^2 B R_L. \tag{A11}$$

In this equation, RIN is the relative intensity noise power spectral density in dB/Hz, $I_{av}$ is the average photocurrent, $B$ is the receiver noise equivalent bandwidth, and $R_L$ is the load resistance. The term $P_{shot}$ is the shot noise power due to the random arrival of photons at the photodetectors, expressed as

$$p_{shot} = 2qr_{PD}p_{av}BR_L, \tag{A12}$$

where $q$ is the electron charge and $P_{av}$ is the average received optical power. The ¼ terms in Eq. (A10) originate from the lossy impedance matching condition at the photodetector. In our experiment, however, we also employed an erbium-doped fiber amplifier (EDFA); therefore, we need to add an additional noise contribution

$$p_N = (1+g)p_{th} + \frac{1}{4}p_{shot} + \frac{1}{4}p_{rin,laser} + \frac{1}{4}p_{EDFA}. \tag{A13}$$

From the definition of noise figure, the noise power from the EDFA is calculated [http://literature.cdn.keysight.com/litweb/pdf/5952-8255E.pdf, from Eqs. (A1)–(A6)] as

$$p_{EDFA} = (F_{EDFA} - 1)g_{EDFA}kTB, \tag{A14}$$

where $F_{EDFA}$ is the noise factor of the EDFA, that is, the noise figure expressed in linear scale.

Now, considering the values of the parameters used in our experimental setup (shown in Table I) and assuming the worst case noise figure for the EDFA (4 dB) from Eqs. (A7)–(A10) above, we calculated the individual noise terms and the total noise power. We report them in Table II.

It appears from Table II that the dominant terms are the relative intensity noise from the laser and the noise generated by the EDFA. At this point, from Eq. (A2), we can calculate the noise figure of our link to be approximately 45.8 dB at 300 GHz. This value can be further reduced by improving the fiber-to-chip coupling scheme that, as mentioned in Sec. II, has not been optimized. With a fiber-to-chip loss reduction from 5 dB to 2.5 dB, the overall noise figure of the link improves from 45.8 dB to 40.3 dB and the link gain improves from −24 dB to −14 dB.

## 4. Spurious-free dynamic range

Based on the noise power, we can now also estimate the spurious-free dynamic range of the link. Very important to this scope are the assumptions made on nonlinear distortions. We start with the hypothesis that nonlinear distortions will stay approximately constant over frequency (as mentioned above, they could not be measured over the range of frequencies where the link operates). In that case, we would observe an input intercept points IP3 of 18.9 dB. This would result in SFDR3 in the order of 92.7 dB/Hz$^{2/3}$ and an SFDR2 in the order of 94.9 dB/Hz$^{1/2}$ (Fig. 6). It is important to note that the SFDR2 can be largely improved by accurately adjusting the bias point to exact quadrature. During the tests, bias voltage was adjusted with a relatively rough resolution of 0.1 V.

**TABLE I**. Parameters employed in the analog photonic link experiment.

| Parameter | Value |
|---|---|
| Link gain | −24 dB |
| Noise equivalent bandwidth | 100 GHz |
| Relative intensity noise of the laser | −155 dB/Hz |
| Photodetector responsivity | 0.24 A/W |
| Noise figure of the EDFA | <4 dB |
| EDFA gain | 24.9 dB |

**TABLE II**. Evaluation of the noise contributions in the photonic link.

| Noise term | Power (logarithmic scale) (dBm/Hz) | Power (linear scale) (W) |
|---|---|---|
| Thermal noise (modulator, $P_{th,MZM}$) | −197.7523 | $1.6779 \times 10^{-12}$ |
| Shot noise ($P_{shot}$) | −163.3311 | $4.622 \times 10^{-9}$ |
| Relative intensity noise ($P_{rin}$) | −152.7666 | $5.2635 \times 10^{-8}$ |
| EDFA noise ($P_{EDFA}$) | −153.28 | $4.6767 \times 10^{-8}$ |
| Thermal noise (photodetector, $P_{th,PD}$) | −173.9752 | $4.0039 \times 10^{-10}$ |
| Total noise power ($P_N$) | −149.8119 | $1.0443 \times 10^{-7}$ |

It is very important to note that the assumption of keeping the same IP3 is very conservative. In fact, the modulator used in the analog link test has a higher $V_{\pi,RF}$ (6.7 V vs 3 V) and a lower loss than the one used in the nonlinear distortion tests. In a Mach-Zehnder modulator based analog optical link, the power of the IMD3 terms reduces as the sixth power of $V_{\pi,RF}$ and as the second power of the loss $L$, according to the equation[14,64]

$$P_{IMD3,MZM} = \frac{1}{2048}\left(\frac{\pi V_m}{V_{\pi,RF}}\right)^6\left(\frac{r_{PD}P_i}{L}\sin\varphi_B\right)^2 R_I. \quad \text{(A15)}$$

Therefore, the level of IMD3 will largely decrease when increasing the $V_{\pi,RF}$, making its dynamic range increase rapidly. In our case, evaluating the previous expression gives a reduction in IMD3 power of 34.5 dB. This results in a much improved SFDR3 of 105.2 dB/Hz$^{2/3}$ and an IIP3 of 38.1 dBm, as shown in Fig. 7. A similar discussion can be made for the power of the IMD2 terms, which follows the relation

$$P_{IMD2,MZM} = \frac{1}{128}\left(\frac{\pi V_m}{V_{\pi,RF}}\right)^4\left(\frac{r_{PD}P_i}{L}\cos\varphi_B\right)^2 R_L. \quad \text{(A16)}$$

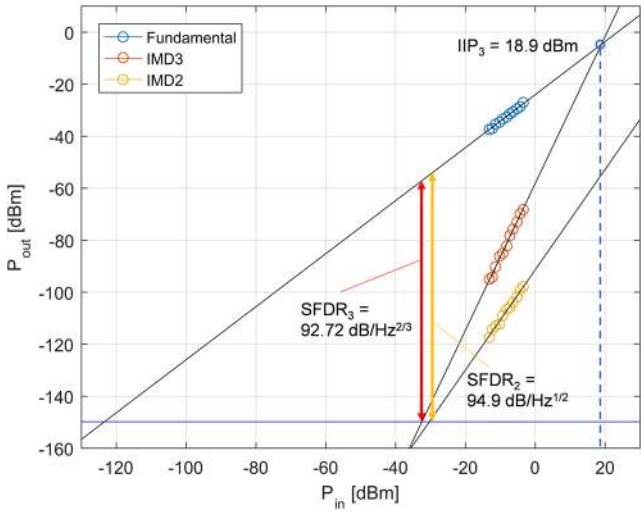


**FIG. 6**. Estimation of spurious-free dynamic range of the 325 GHz analog photonic link.

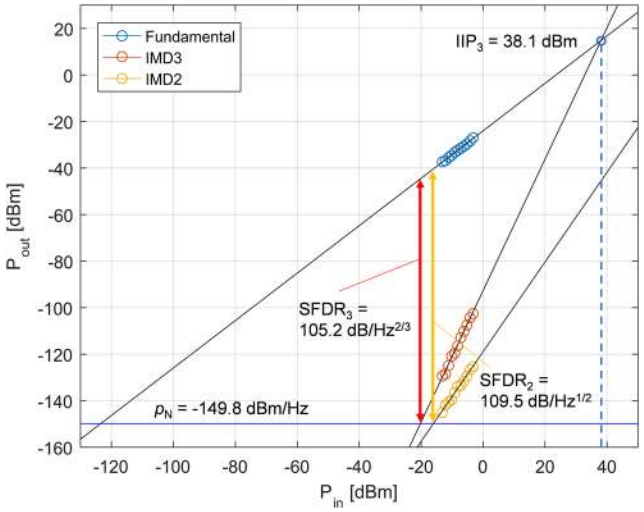


**FIG. 7**. Estimation of spurious-free dynamic range of the 325 GHz analog photonic link, including the reduction IMD3 and IMD2 estimated on the basis of the measured parameters of the modulator.

In this case, the IMD2 power reduces by 27.6 dB, and the SFDR2 increases to 109.48 dB/Hz$^{1/2}$. These results are shown in Fig. 7.

## REFERENCES


[1] A. J. Seeds, H. Shams, M. J. Fice *et al.*, "TeraHertz photonics for wireless communications," J. Lightwave Technol. **33**(3), 579–587 (2015).

[2] J. Federici and L. Moeller, "Review of terahertz and subterahertz wireless communications," J. Appl. Phys. **107**(11), 111101 (2010).

[3] H. J. Song and T. Nagatsuma, "Present and future of terahertz communications," IEEE Trans. Terahertz Sci. Technol. **1**(1), 256–263 (2011).

[4] T. Nagatsuma, S. Horiguchi, Y. Minamikata *et al.*, "Terahertz wireless communications based on photonics technologies," Opt. Express **21**(20), 23736–23747 (2013).

[5] S. Jia, X. Pang, O. Ozolins *et al.*, "0.4 THz photonic-wireless link with 106 Gb/s single channel bitrate," J. Lightwave Technol. **36**(2), 610–616 (2018).

[6] See http://literature.cdn.keysight.com/litweb/pdf/5989-2923EN.pdf for Millimeter-Wave Source Modules, Keysight Technologies, mm-wave Source Modules.

[7] See https://www.vadiodes.com/en/products/signal-generator for Signal Generator Extension Modules, Virginia Diodes, Signal Generator Extension Modules.

[8] L. K. Oxenløwe, S. Jia, X. Pang, O. Ozolins, X. Yu, H. Hu, P. Guan, F. Da Ros, S. Popov, G. Jacobsen, M. Galili, D. Zibar, and T. Morioka, "100s Gigabit/s THz communication," in *Conference on Lasers and Electro-Optics, OSA Technical Digest* (Optical Society of America, 2018), paper STu3D.1 (published online).

[9] Y. Salamin, P. Ma, B. Baeuerle *et al.*, "100 GHz plasmonic photodetector," ACS Photonics **5**(8), 3291–3297 (2018).

[10] B. Khani, S. Makhlouf, A. Steffan, J. Honecker, and A. Stöhr, "Planar 0.05–1.1 THz laminate-based transition designs for integrating high-frequency photodiodes with rectangular waveguides," J. Lightwave Technol. **37**(3), 1037–1044 (2019).

[11] Y. Salamin, W. Heni, C. Haffner *et al.*, "Direct conversion of free space millimeter waves to optical domain by plasmonic modulator antenna," Nano Lett. **15**(12), 8342–8346 (2015).

[12] X. Zhang, A. Hosseini, H. Subbaraman *et al.*, "Integrated photonic electromagnetic field sensor based on broadband bowtie antenna coupled silicon organic hybrid modulator," J. Lightwave Technol. **32**(20), 3774–3784 (2014).

[13]Y. Salamin, B. Baeuerle, W. Heni *et al.*, "Microwave plasmonic mixer in a transparent fibre–wireless link," Nat. Photonics **12**(12), 749–753 (2018).
[14]C. H. Cox, *Analog Optical Links: Theory and Practice* (Cambridge University Press, 2006).
[15]R. DeSalvo, C. Middleton, E. Grafer *et al.*, "The convergence of microwave photonic and optical wireless systems with military communication and sensor systems," in *2016 IEEE Avionics and Vehicle Fiber-Optics and Photonics Conference (AVFOP), Long Beach, CA, 31 October–3 November 2016* (IEEE, 2016), pp. 191–192.
[16]S. Hughes, J. S. Langston, R. DeSalvo, C. Middleton, E. Grafer, S. E. Ralph, and A. J. Stark, "Agile micro- and millimeter-wave communication using photonic frequency conversion," in *Optical Fiber Communication Conference, OSA Technical Digest* (Optical Society of America, 2016), paper W1G.5 (published online).
[17]R. Palacio, F. Deborgies, and P. Piironen, "Optical distribution of microwave signals for Earth observation satellites," in *2010 IEEE International Topical Meeting on Microwave Photonics, Montreal, QC, 5–9 October 2010* (IEEE, 2010), pp. 74–77.
[18]W. Liu, M. Li, R. S. Guzzon *et al.*, "A fully reconfigurable photonic integrated signal processor," Nat. Photonics **10**, 190 (2016).
[19]A. Kanno, "High bitrate mm-wave links using RoF technologies and its non-telecom application," in *Optical Fiber Communication Conference, OSA Technical Digest* (Optical Society of America, 2017), paper Th4E.6 (published online).
[20]P. Ghelfi, F. Laghezza, F. Scotti *et al.*, "A fully photonics-based coherent radar system," Nature **507**, 341 (2014).
[21]E. I. Ackerman, G. E. Betts, and C. H. Cox, "Inherently broadband linearized modulator for high-SFDR, low-NF microwave photonic links," in *2016 IEEE International Topical Meeting on Microwave Photonics (MWP), Long Beach, CA, 31 October–3 November 2016* (IEEE, 2016), pp. 265–268.
[22]R. G. Walker, N. I. Cameron, Y. Zhou *et al.*, "Optimized gallium arsenide modulators for advanced modulation formats," IEEE J. Sel. Top. Quantum Electron. **19**(6), 138–149 (2013).
[23]J. Yu, C. Rolland, D. Yevick *et al.*, "A novel method for improving the performance of InP/InGaAsP multiple-quantum-well mach-Zehnder modulators by phase shift engineering," OSA Technical Digest Series 6, ITuG4, 1996.
[24]C. Zhang, P. A. Morton, J. B. Khurgin *et al.*, "Highly linear heterogeneous-integrated Mach-Zehnder interferometer modulators on Si," Opt. Express **24**(17), 19040–19047 (2016).
[25]P. O. Weigel, J. Zhao, K. Fang *et al.*, "Bonded thin film lithium niobate modulator on a silicon photonics platform exceeding 100 GHz 3-dB electrical modulation bandwidth," Opt. Express **26**(18), 23728–23739 (2018).
[26]A. J. Mercante, S. Shi, P. Yao *et al.*, "Thin film lithium niobate electro-optic modulator with terahertz operating bandwidth," Opt. Express **26**(11), 14810–14816 (2018).
[27]C. Wang, M. Zhang, X. Chen *et al.*, "Integrated lithium niobate electro-optic modulators operating at CMOS-compatible voltages," Nature **562**(7725), 101–104 (2018).
[28]D. Marpaung, J. Yao, and J. Capmany, "Integrated microwave photonics," Nat. Photonics **13**(2), 80–90 (2019).
[29]C. Haffner, D. Chelladurai, Y. Fedoryshyn *et al.*, "Low-loss plasmon-assisted electro-optic modulator," Nature **556**(7702), 483–486 (2018).
[30]B. Baeuerle *et al.*, "Plasmonic-organic hybrid modulators for optical interconnects beyond 100G/λ," 2018 Conference on Lasers and Electro-Optics (CLEO), San Jose, CA, 2018, pp. 1–2, see http://ieeexplore.ieee.org/stamp/stamp.jsp?tp=&arnumber=8427719&isnumber=8426208.
[31]C. Hoessbacher, A. Josten, B. Baeuerle *et al.*, "Plasmonic modulator with >170 GHz bandwidth demonstrated at 100 GBd NRZ," Opt. Express **25**(3), 1762–1768 (2017).
[32]S. Ummethala, T. Harter, K. Köhnle, S. Muehlbrandt, Y. Kutuvantavida, J. N. Kemal, J. Schaefer, H. Massler, A. Tessmann, S. K. Garlapati, A. Bacher, L. Hahn, M. Walther, T. Zwick, S. Randel, W. Freude, and C. Koos, "Terahertz-to-optical conversion using a plasmonic modulator," in *Conference on Lasers and Electro-Optics, OSA Technical Digest* (Optical Society of America, 2018), paper STu3D.4 (published online).
[33]C. Haffner, W. Heni, Y. Fedoryshyn *et al.*, "All-plasmonic Mach–Zehnder modulator enabling optical high-speed communication at the microscale," Nat. Photonics **9**(8), 525–528 (2015).
[34]I.-C. Benea-Chelmus, T. Zhu, F. F. Settembrini *et al.*, "Three-dimensional phase modulator at telecom wavelength acting as a terahertz detector with an electro-optic bandwidth of 1.25 terahertz," ACS Photonics **5**(4), 1398–1403 (2018).
[35]T. Nikolajsen, K. Leosson, and S. I. Bozhevolnyi, "Surface plasmon polariton based modulators and switches operating at telecom wavelengths," Appl. Phys. Lett. **85**(24), 5833–5835 (2004).
[36]H. A. Atwater, "The promise of plasmonics," Sci. Am. **296**(4), 56–62 (2007).
[37]W. Cai, J. S. White, and M. L. Brongersma, "Compact, high-speed and power-efficient electrooptic plasmonic modulators," Nano Lett. **9**(12), 4403–4411 (2009).
[38]W. Heni, Y. Kutuvantavida, C. Haffner *et al.*, "Silicon–organic and plasmonic–organic hybrid photonics," ACS Photonics **4**(7), 1576–1590 (2017).
[39]W. Heni, C. Haffner, D. L. Elder *et al.*, "Nonlinearities of organic electro-optic materials in nanoscale slots and implications for the optimum modulator design," Opt. Express **25**(3), 2627–2653 (2017).
[40]D. L. Elder, C. Haffner, W. Heni *et al.*, "Effect of rigid bridge-protection units, quadrupolar interactions, and blending in organic electro-optic chromophores," Chem. Mater. **29**(15), 6457–6471 (2017).
[41]R. W. Boyd, *Nonlinear Optics* (Academic Press, 2003).
[42]C. Haffner, W. Heni, Y. Fedoryshyn *et al.*, "Plasmonic organic hybrid modulators—Scaling highest speed photonics to the microscale," Proc. IEEE **104**(12), 2362–2379 (2016).
[43]C. Hoessbacher, *Plasmonic Switches and Modulators for Optical Communications* (ETH Zurich, Zurich, Switzerland, 2017).
[44]W. Heni, C. Haffner, B. Baeuerle *et al.*, "108 Gbit/s plasmonic Mach-Zehnder modulator with >70-GHz electrical bandwidth," J. Lightwave Technol. **34**(2), 393–400 (2016).
[45]C. Haffner, W. Heni, D. L. Elder *et al.*, "Harnessing nonlinearities near material absorption resonances for reducing losses in plasmonic modulators," Opt. Mater. Express **7**(7), 2168–2181 (2017).
[46]J. Tian, S. Yu, W. Yan *et al.*, "Broadband high-efficiency surface-plasmon-polariton coupler with silicon-metal interface," Appl. Phys. Lett. **95**(1), 013504 (2009).
[47]L. Alloatti, D. Korn, R. Palmer *et al.*, "42.7 Gbit/s electro-optic modulator in silicon technology," Opt. Express **19**(12), 11841–11851 (2011).
[48]E. I. Ackerman and C. H. Cox, "RF fiber-optic link performance," IEEE Microwave Mag. **2**(4), 50–58 (2001).
[49]V. J. Urick, M. S. Rogge, F. Bucholtz *et al.*, "Wideband (0.045–6.25 GHz) 40 km analogue fibre-optic link with ultra-high (>40 dB) all-photonic gain," Electron. Lett. **42**(9), 552–553 (2006).
[50]D. Marpaung, C. Roeloffzen, R. Heideman *et al.*, "Integrated microwave photonics," Laser Photonics Rev. **7**(4), 506–538 (2013).
[51]S. Iezekiel, M. Burla, J. Klamkin *et al.*, "RF engineering meets optoelectronics: Progress in integrated microwave photonics," IEEE Microwave Mag. **16**(8), 28–45 (2015).
[52]M. Burla, X. Wang, M. Li *et al.*, "Wideband dynamic microwave frequency identification system using a low-power ultracompact silicon photonic chip," Nat. Commun. **7**, 13004 (2016).
[53]L. M. Zhuang, D. Marpaung, M. Burla *et al.*, "Low-loss, high-index-contrast $Si_3N_4/SiO_2$ optical waveguides for optical delay lines in microwave photonics signal processing," Opt. Express **19**(23), 23162–23170 (2011).
[54]J. Capmany, I. Gasulla, and D. Pérez, "The programmable processor," Nat. Photonics **10**, 6 (2016).
[55]J. S. Fandiño and P. Muñoz, "Photonics-based microwave frequency measurement using a double-sideband suppressed-carrier modulation and an In P integrated ring-assisted Mach–Zehnder interferometer filter," Opt. Lett. **38**(21), 4316–4319 (2013).
[56]D. Marpaung, B. Morrison, R. Pant *et al.*, "$Si_3N_4$ ring resonator-based microwave photonic notch filter with an ultrahigh peak rejection," Opt. Express **21**(20), 23286–23294 (2013).

[57]L. Zhuang, C. G. H. Roeloffzen, M. Hoekman *et al.*, "Programmable photonic signal processor chip for radiofrequency applications," Optica **2**(10), 854–859 (2015).
[58]D. Pérez, I. Gasulla, L. Crudgington *et al.*, "Multipurpose silicon photonics signal processor core," Nat. Commun. **8**(1), 636 (2017).
[59]J. S. Fandiño, P. Muñoz, D. Doménech *et al.*, "A monolithic integrated photonic microwave filter," Nat. Photonics **11**, 124 (2016).
[60]A. Meijerink, C. G. H. Roeloffzen, R. Meijerink *et al.*, "Novel ring resonator-based integrated photonic beamformer for broadband phased array receive antennas—Part I: Design and performance analysis," J. Lightwave Technol. **28**(1), 3–18 (2010).
[61]D. M. Pozar, *Microwave Engineering* (John Wiley & Sons, 2009).
[62]C. Uhl, H. Hettrich, and M. Möller, "Design considerations for a 100 Gbit/s SiGe–BiCMOS power multiplexer with 2 $V_{pp}$ differential voltage swing," IEEE J. Solid-State Circuits **53**(9), 2479–2487 (2018).
[63]C. Uhl, H. Hettrich, and M. Möller, "A 100 Gbit/s 2 Vpp power multiplexer in SiGe BiCMOS technology for directly driving a monolithically integrated plasmonic MZM in a silicon photonics transmitter," in *2017 IEEE Bipolar/BiCMOS Circuits and Technology Meeting (BCTM), Miami, FL, 19–21 October 2017* (IEEE, 2017), pp. 106–109.
[64]D. A. I. Marpaung, *High Dynamic Range Analog Photonic Links: Design and Implementation* (Twente University Press, Enschede, The Netherlands, 2009).